

How much gas and dust is in the $z = 5.7$ Lyman Break Galaxy HZ10?

An ALMA Band 10 to 4 and JWST/NIRSpec study of its interstellar medium

H. S. B. Algera^{1*}, R. Herrera-Camus^{2,3*}, M. Aravena^{4,3}, R. Assef⁴, T. L. J. C. Bakx⁵, A. Bolatto⁶, K. Cescon⁷, C.-C. Chen¹, E. da Cunha⁸, P. Dayal^{9,10,11}, I. De Looze¹², T. Diaz-Santos^{13,14}, A. Faisst¹⁵, A. Ferrara¹⁶, N. Förster Schreiber¹⁷, N. Hathi¹⁸, R. Ikeda^{19,20}, H. Inami²¹, G. C. Jones^{22,23}, A. Koekemoer¹⁸, D. Lutz²⁴, M. Relaño^{25,26}, M. Romano^{27,28}, L. Rowland⁷, L. Sommovigo²⁹, L. Vallini³⁰, A. Vijayan³¹, V. Villanueva², and P. van der Werf⁷

(Affiliations can be found after the references)

Received -; accepted -

ABSTRACT

Context. A complete overview of the stellar, gas and dust contents of galaxies is key to understanding their assembly at early times. However, an estimation of molecular and atomic gas reservoirs at high redshift relies on various indirect tracers, while robust dust mass measurements require multi-band far-infrared continuum observations.

Aims. We take census of the full baryonic content of the main-sequence star-forming galaxy HZ10 at $z = 5.65$, a unique case study where all necessary tracers are available.

Methods. We present new ALMA Band 10 ($\lambda_{\text{rest}} \approx 50 \mu\text{m}$) and Band 4 ($\approx 300 \mu\text{m}$) observations towards HZ10, which combined with previously taken ALMA Band 6 through 9 data ($\approx 70\text{--}200 \mu\text{m}$) constrains its dust properties. We complete the baryonic picture using archival high-resolution [C II] observations that provide both a dynamical mass and molecular and atomic gas mass estimates, a JVLA CO(2-1)-based molecular gas mass, and JWST metallicity and stellar mass measurements.

Results. We detect continuum emission from HZ10 in Bands 10 and 4 at the $3.4\text{--}4.0\sigma$ level, and measure a dust temperature of $T_{\text{dust}} = 37^{+6}_{-5}$ K and dust mass $\log(M_{\text{dust}}/M_{\odot}) = 8.0 \pm 0.1$. Leveraging the dynamical constraints, we infer its total gas budget, and find that commonly used [C II]-to- H_2 and [C II]-to-HI conversions overpredict the gas mass relative to the dynamical mass. For this reason, we derive a [C II]-to-total ISM mass (atomic + molecular) conversion factor, which for HZ10 corresponds to $\alpha_{\text{[CII]}}^{\text{ISM}} = 39^{+50}_{-25} M_{\odot} L_{\odot}^{-1}$. We also find that HZ10 falls below the local scaling relation between dust-to-gas ratio and metallicity, suggesting inefficient ISM dust growth.

Conclusions. These results demonstrate a powerful synergy between ALMA and JWST in disentangling the baryonic components of early galaxies, paving the way for future studies of larger samples to dynamically calibrate [C II]-to-gas mass conversion factors, and further unravel the pathways of early dust build-up.

Key words. galaxies: evolution – galaxies: high-redshift – galaxies: ISM

1. Introduction

The evolution of galaxies is driven by both dark matter, which establishes the initial gravitational potential that accretes primordial gas, and baryonic matter, whose complex interplay leads to star formation. A complete census of the baryonic components—gas, dust, and stars—is therefore essential to understanding galaxy evolution across cosmic time.

The atomic and molecular gas components play a central role in this process, serving as the raw material for star formation (e.g., Kennicutt & Evans 2012; Krumholz 2012). The atomic gas reservoir can be directly traced by the 21 cm emission line of neutral hydrogen (HI), but this line becomes inaccessible due to instrumental limitations already at $z \gtrsim 0.5\text{--}1$ (e.g., Fernández et al. 2016). Molecular hydrogen, the dominant form of molecular gas and the direct fuel for star formation, is commonly traced by low- J rotational transitions of carbon monoxide (CO). However, CO-based gas mass estimates depend on the CO-to- H_2 conversion factor (α_{CO}), which is known to vary with metallicity and gas density (e.g., Bolatto et al. 2013; Chiang et al. 2024; Teng et al. 2024). In low-metallicity environments, CO emission may be weak or absent due to photodissociation, leaving a significant fraction of molecular gas undetectable in CO-based studies, commonly referred to as “CO-faint” or “CO-dark” molecular gas (e.g., Wolfire et al. 2010; Madden et al. 2020). At high

redshift, CO is furthermore difficult to detect against the warm Cosmic Microwave Background (CMB; da Cunha et al. 2013; Frias Castillo et al. 2024).

The [C II] 158 μm fine-structure line is expected to trace both atomic and molecular gas in galaxies, with a minor fraction of [C II] emission moreover thought to arise from the ionized interstellar medium (ISM; e.g., Croxall et al. 2017; Díaz-Santos et al. 2017; Zhao et al. 2024). Given its typical brightness and multi-phase origin, [C II] is a particularly valuable tool for studying the ISM of high-redshift systems, where direct observations of CO and H I are often challenging. For instance, Heintz et al. (2021) used H I absorption in γ -ray burst host galaxies at $z \gtrsim 2$ to directly measure the [C II]-to-H I conversion factor (β_{HI}). For molecular gas, various methods have been employed to derive a [C II]-to- H_2 conversion factor in both low-metallicity galaxies (e.g., Accurso et al. 2017; Jameson et al. 2018; Madden et al. 2020; Hunt et al. 2023) and high-redshift systems (e.g., Zanella et al. 2018; Pavesi et al. 2019; Dessauges-Zavadsky et al. 2020). At the same time, various theoretical works have tried to calibrate [C II] as a tracer of both H_2 and H I in simulations (Vizgan et al. 2022a,b; Gurman et al. 2024; Casavecchia et al. 2025; Vallini et al. 2025). Observational studies generally find that galaxies at $z \gtrsim 4$ are rich in both atomic and molecular gas (e.g., Dessauges-Zavadsky et al. 2020; Heintz et al. 2021; Aravena et al. 2024), similar to those at cosmic noon (e.g., Scoville et al. 2017; Tacconi et al. 2018, 2020). However, discrepan-

* Both authors contributed equally to this work.

cies between different calibrations and methodologies remain a major source of uncertainty, and until recently, no simultaneous calibrations existed for atomic and molecular gas in high-redshift galaxies (c.f., the theoretical works by Casavecchia et al. 2025; Vallini et al. 2025). In this context, detailed observations of high-redshift systems—where baryonic mass can be inferred from kinematics alongside independent measurements of gas mass, stellar mass, and metallicity—are crucial for improving the accuracy of these estimates.

Dust—despite being negligible in terms of the total mass budget—is another important baryonic component in galaxies due to its significant effect on their observable spectral energy distribution (SED), and importance in catalyzing the formation of molecular hydrogen (e.g., Galliano et al. 2018). Recent observations with the Atacama Large Millimeter/submillimeter Array (ALMA) have revealed the widespread presence of dust in the early Universe ($z \gtrsim 6$; e.g., Tamura et al. 2019; Inami et al. 2022). However, to understand the exact pathways of early dust production, it is essential to precisely constrain the dust masses of high-redshift galaxies through multi-band ALMA continuum observations. In particular, observations probing both the peak and Rayleigh-Jeans tail of the dust SED are crucial to break degeneracies between the dust mass, temperature and emissivity index of high-redshift galaxies (e.g., Bakx et al. 2021; da Cunha et al. 2021; Algera et al. 2024a). Covering the peak of the SED requires dedicated high-frequency observations, for which ALMA Band 9 – tracing rest-frame $\lambda \lesssim 80 \mu\text{m}$ at $z \gtrsim 5$ – has recently been employed to great effect (e.g., Bakx et al. 2021, 2025; Algera et al. 2024a; Tripodi et al. 2024; Villanueva et al. 2024). However, to obtain the most stringent constraints it is necessary to sample beyond the peak, requiring observations in the under-exploited ALMA Band 10 (e.g., Fernández Aranda et al. 2025).

Further insight into dust production mechanisms requires knowledge of galaxy metallicities, as metallicity appears to drive the dust-to-gas and dust-to-metal ratios of galaxies in the nearby Universe (e.g., Fisher et al. 2014; Rémy-Ruyer et al. 2014; De Vis et al. 2019; De Looze et al. 2020; Galliano et al. 2021). In particular, at low metallicities dust is thought to predominantly be produced by stellar sources—supernovae (SNe) and AGB stars—while at higher metallicities dust growth in the dense ISM likely takes over (e.g., Inoue 2011; Asano et al. 2013; Feldmann 2015; Popping et al. 2017; Galliano et al. 2021; Choban et al. 2024; Sawant et al. 2025). With the advent of the *James Webb Space Telescope* (JWST), the first metallicity measurements of dusty galaxies at $z \gtrsim 6$ have now become available (e.g., Valentino et al. 2024; Rowland et al. 2025b) and enable testing these low-redshift scaling relations at an epoch where dust has had significantly less time to form. The high dust masses and metallicities of UV-luminous galaxies at $z \sim 7$ suggest rapid dust build-up through a combination of SNe and ISM dust growth (Algera et al. 2025), although galaxies at even higher redshifts show lower dust-to-stellar mass ratios suggesting limited growth in the ISM (Ciesla et al. 2024; Algera et al. 2025; Burgarella et al. 2025; Ferrara et al. 2025; Mitsuhashi et al. 2025; see also Ferrara et al. 2016 for a theoretical perspective on why ISM growth may be inhibited at early times). Larger galaxy samples with well-constrained dust masses from multi-band ALMA observations are required to more accurately test theoretical models of early dust production.

In this paper, we present the case study of HZ10, one of the best examples—if not the best—for examining the total mass budget in a normal, star-forming galaxy at $z \sim 6$. This is partly because HZ10 is, to date, the only main-sequence galaxy at this cosmic epoch with a combination of: (i) a direct detection of molecular gas via a low- J CO transition (CO(2-1); Pavesi et al. 2019), (ii) a robust dynamical mass estimate based on detailed kinematic modeling of its [C II] line emission (Telikova et al. 2024), (iii) a multi-band dust SED (this work; Faisst et al. 2020;

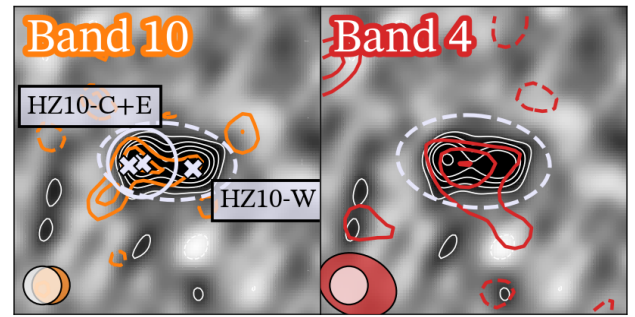


Fig. 1. The new ALMA observations of HZ10 presented in this work. (Left): ALMA Band 10 contours (orange) on top of the ALMA Band 9 continuum imaging presented in Villanueva et al. (2024, background greyscale and white contours). The centroids of the central (C) and western (W) components as identified via [C II] emission in Telikova et al. (2024) are annotated. We moreover show the center of the eastern component (E) identified in JWST/NIRSpec by Jones et al. (2024), although it is fully blended with HZ10-C at the resolution of the ALMA observations. (Right): ALMA Band 4 contours (red) on top of the ALMA Band 9 map. Both cutouts span $4'' \times 4''$, and beam sizes are shown in the lower left corner. Contours are placed at $\pm 1\sigma$ intervals starting from $\pm 2\sigma$ with negative contours being dashed. Band 10 (4) continuum emission is detected at the 3.4σ (4.0σ) level. We extract the Band 10 and 4 flux densities of the full HZ10 system in the dashed apertures, avoiding a likely noise spike to the south-east in the Band 10 map. We extract the Band 10 flux density of HZ10-C+E in the smaller circular aperture.

Villanueva et al. 2024), and (iv) a metallicity measurement from JWST/NIRSpec observations (Jones et al. 2024).

Throughout this work, we assume a standard flat Λ CDM cosmology with $\Omega_m = 1 - \Omega_\Lambda = 0.30$ and $H_0 = 70 \text{ km/s/Mpc}$. At the redshift of HZ10, $z = 5.65$, 1 arcsec corresponds to 5.9 kpc. We moreover assume a Chabrier (2003) initial mass function (IMF).

2. Target and data

2.1. HZ10

In this work, we present new ALMA Band 10 and 4 observations towards the massive ($\log(M_\star/M_\odot) = 10.35 \pm 0.37$; Mitsuhashi et al. 2024) Lyman-break galaxy HZ10 in the COSMOS field (Scoville et al. 2007). The redshift of HZ10 was initially measured spectroscopically via a detection of its Lyman- α emission ($z_{\text{Ly}\alpha} = 5.659 \pm 0.004$) through Keck/DEIMOS observations, and the galaxy was subsequently followed up by ALMA in [C II] $158 \mu\text{m}$ ($z_{[\text{C II}]} = 5.6566 \pm 0.0002$) and underlying dust continuum emission in Band 7 (Capak et al. 2015). Among the nine $z \sim 5 - 6$ galaxies in the Capak et al. sample, HZ10 turned out to be the most FIR-luminous continuum source, as well as one of the brightest [C II] emitters. This motivated follow-up observations of its CO(2-1) line using the Very Large Array (VLA) by Pavesi et al. (2019), who detected the line at $> 8\sigma$ significance. The CO(2-1) detection in HZ10 represents one of the most distant detections of molecular gas in a main-sequence galaxy to date (c.f., D’Odorico et al. 2018; Zavala et al. 2022).

To study its dust continuum emission, Faisst et al. (2020) presented additional ALMA Band 6 and 8 observations towards HZ10. From a modified blackbody fit including the aforementioned Band 7 data, they determined its dust temperature and infrared luminosity to be $T_{\text{dust}} = 46^{+16}_{-8} \text{ K}$ and $\log(L_{\text{IR}}/L_\odot) = 12.5^{+0.1}_{-0.3}$, respectively, suggesting HZ10 to be an Ultra-luminous Infrared Galaxy (ULIRG; defined as having $L_{\text{IR}} > 10^{12} L_\odot$). New ALMA Band 9 observations, which better capture the peak of the

infrared emission, were recently presented by Villanueva et al. (2024). They refined the constraints on the dust SED of HZ10, finding a dust temperature of $T_{\text{dust}} = 47 \pm 7$ K, consistent with Faist et al. (2020).

Recent observations of HZ10 with *JWST*/NIRSpec as part of the GA-NIFS program were presented by Jones et al. (2024). Their observations reveal a clumpy, three-component structure: a main component (HZ10-C) separated from a second minor component (HZ10-E) by only ~ 1.6 kpc, and a third component (HZ10-W) separated by ~ 3.6 kpc. Telikova et al. (2024), using high-resolution ($\theta \approx 0''.3$) ALMA [C II] observations, find evidence that the HZ10-C+E components correspond to a disturbed rotating disk with a rotational support of $V_{\text{rot}}/\sigma_0 \approx 2$. The western component, HZ10-W, is both fainter in [C II] emission and more compact, preventing a similarly detailed kinematic analysis. Finally, based on various emission line ratios, Jones et al. (2024) find that HZ10 is primarily powered by star formation, and has a gas-phase metallicity of $Z \approx 0.52 - 0.71 Z_{\odot}$ across the three components (HZ10-C, -E and -W). Based on their findings, we adopt a metallicity of $Z/Z_{\odot} = 0.6 \pm 0.1$ in our analysis, both for HZ10 as a whole, and for the rotationally-supported HZ10-C+E system.

2.2. New ALMA Band 4 and 10 observations

We present new ALMA Band 10 (0.35 mm) and Band 4 (2 mm) observations towards HZ10, taken as part of projects 2024.1.01134.S (PI Herrera-Camus) and 2023.1.01033.S (PI Algera), respectively. These new observations are shown in Figure 1, where they are overlaid on the ALMA Band 9 image presented in Villanueva et al. (2024).

The primary goal of the Band 4 observations was to probe the Rayleigh-Jeans tail of the dust emission and thereby improve the constraints on the dust mass and emissivity index of HZ10. Owing to its brightness, a short integration time of $t_{\text{int}} \approx 300$ s was adopted in Band 4. The calibrated visibility data were restored in CASA version 6.5.4 (McMullin et al. 2007; CASA Team et al. 2022) following the standard approach using `SCRIPTFORPL.PY`. We confirmed that the CO(8-7) line, redshifted to $\nu_{\text{obs}} = 138.47$ GHz, was not detected, and therefore all channels were included in the imaging. We adopted natural weighting to maximize sensitivity, yielding a beam size of $1''.06 \times 0''.81$ and a root-mean-square (rms) sensitivity of $\sigma = 30.4 \mu\text{Jy beam}^{-1}$. Continuum emission from HZ10 is detected at the $\sim 4.0\sigma$ level, with the peak of the emission being located in between the central (C+E) and western (W) components of the galaxy.

The primary goal of the ALMA Band 10 observations was to detect the [OIII] $52 \mu\text{m}$ transition, and the results will be presented in Herrera-Camus et al. (in preparation). The total Band 10 integration time was $t_{\text{int}} = 154.3$ min. The calibrated visibility data were restored in CASA version 6.6 following the standard approach using `SCRIPTFORPL.PY`. Using natural weighting, the Band 10 image attains a sensitivity of $\sigma = 536 \mu\text{Jy beam}^{-1}$ with a beam size of $0''.38 \times 0''.35$. However, we opt to use a Band 10 image tapered to a circular beam of $0''.5$ to avoid over-resolving the emission of HZ10 and to match the resolution of the Band 9 data. We detect a $\sim 3.4\sigma$ signal coincident with the position of HZ10-C+E, and a further $\sim 2\sigma$ elongated feature stretching out to HZ10-W. Moreover, we observe a $\sim 3\sigma$ emission feature stretching out from HZ10-C+E towards the south-east. As the significantly deeper Band 9 data do not show any signal at this location, we deem it to be a noise spike.

2.3. Flux density measurements

We extract the flux density of the entire HZ10 system in the elliptical apertures shown in Fig. 1 (Bands 10 and 4) and Fig. A.1 (all bands). The resulting measurements are provided in Table

Table 1. Optically thin modified blackbody fitting results for the integrated photometry and resolved C+E components of HZ10.

| | HZ10 | HZ10-C+E |
|-------------------------------------|----------------|----------------|
| $\log(M_{\text{dust}}/M_{\odot})$ | 8.0 ± 0.1 | 7.9 ± 0.2 |
| T_{dust} [K] | 37^{+6}_{-5} | 37^{+6}_{-5} |
| β_{IR} | 2.2 ± 0.4 | 2.1 ± 0.4 |
| $\lambda_{\text{peak}}/\mu\text{m}$ | 76^{+7}_{-6} | 78^{+8}_{-7} |
| $\log(L_{\text{IR}}/L_{\odot})$ | 12.4 ± 0.1 | 12.1 ± 0.1 |

B.1 in Appendix B. We verify that the flux densities measured in Bands 6, 7, 8 and 9 are consistent with previous works (Faist et al. 2020; Villanueva et al. 2024). The high angular resolution of the observations in Bands 7, 9 and 10 moreover enables a flux density measurement of just HZ10-C+E, the rotationally supported component of the HZ10 system. We extract these measurements in a smaller aperture centered on the centroid of the [C II] emission of HZ10-C+E reported in Telikova et al. (2024).

To account for systematic uncertainties in the ALMA flux scale, we add additional calibration uncertainties in quadrature to the measurement errors, following the ALMA technical handbook.¹ For ALMA Band 4 (Bands 6, 7 and 8), we adopt a 5% (10%) calibration uncertainty, while for Bands 9 and 10 we adopt a larger recommended systematic error of 20%.

3. Results

The left panel of Figure 2 shows a composite image of HZ10 combining ALMA continuum observations from Bands 4, 7, and 9. In this image, we clearly distinguish the two main components, HZ10-C+E and HZ10-W. As shown by the beam size achieved in the different ALMA bands at the bottom of the figure, only the Band 7 and Band 9 observations spatially resolve HZ10 (Villanueva et al. 2024; Telikova et al. 2024). Thus, to incorporate the Band 4 observations into the dust SED modeling, we first focus on the source-integrated properties of HZ10. For completeness, we also present the images in all of Bands 10 - 4 in Figure A.1 in Appendix A, and provide the flux measurements as well as other relevant physical parameters in Table B.1 in Appendix B.

We fit the source-integrated continuum photometry of HZ10 with a single-temperature, optically thin modified blackbody (MBB; right panel of Fig. 2), following the fitting framework introduced in Algera et al. (2024b). We leave the dust mass, temperature and emissivity index as free parameters and adopt flat priors on $\log(M_{\text{dust}}/M_{\odot})$ and T_{dust} following Algera et al. (2024b,a). Given the relatively low S/N of the Band 4 detection, we adopt a Gaussian prior on β_{IR} with a mean (standard deviation) of 2.0 (0.5). This range is consistent with recent determinations of β_{IR} in submillimeter galaxies (e.g., da Cunha et al. 2021; Liao et al. 2024; Bendo et al. 2025), as well as in galaxies and quasars at $z \gtrsim 4$ (Witstok et al. 2023; Algera et al. 2024a; Tripodi et al. 2024). A dust mass opacity coefficient κ_{ν} at rest-frame $850 \mu\text{m}$ of $\kappa_{850} = 0.77 \text{ g}^{-1} \text{ cm}^2$ is assumed, following Dunne et al. (2000). The effect of the CMB is moreover included in the fit, following da Cunha et al. (2013), and dust temperatures and IR luminosities are quoted as if at $z = 0$ (i.e., subject to a CMB temperature of 2.73 K).

We adopt the median and 16 – 84th percentiles as the ‘best fit’ and corresponding uncertainty, respectively, and present the results in Table 1. From the fit, we infer a dust temperature of $T_{\text{dust}} = 37^{+6}_{-5}$ K, a dust mass of $\log(M_{\text{dust}}/M_{\odot}) = 8.0 \pm 0.1$, and

¹ <https://almascience.nao.ac.jp/documents-and-tools/cycle11/alma-technical-handbook>

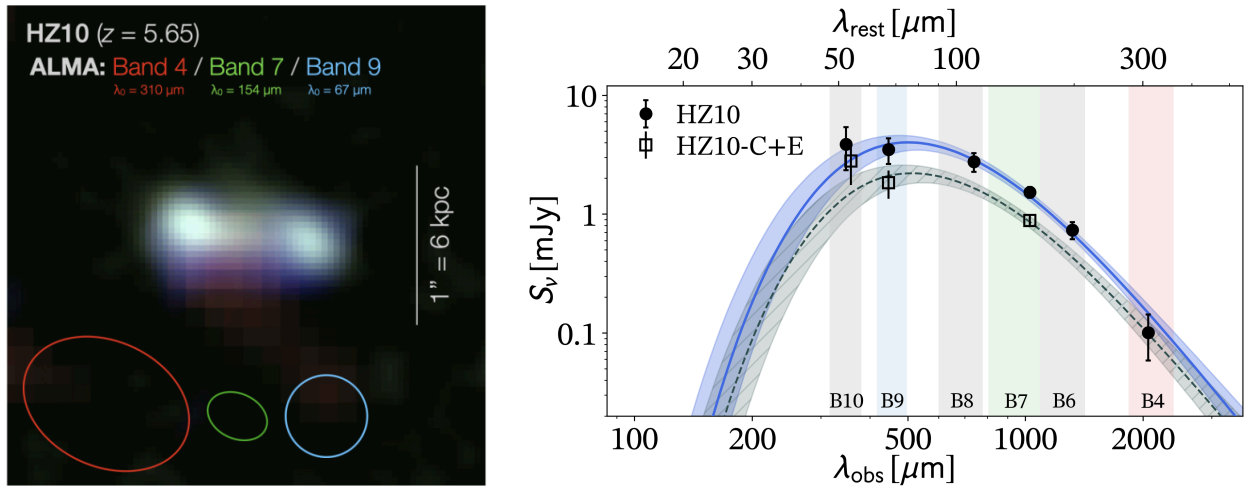


Fig. 2. (*Left*): Composite image of HZ10 combining ALMA continuum observations from Band 4 (red), Band 7 (green), and Band 9 (blue). The beam sizes for each ALMA band are shown at the bottom, and the physical scale is indicated on the right. (*Right*): Our fiducial optically thin modified blackbody fits to the multi-band ALMA photometry of HZ10 (black circles and blue shading) and HZ10-C+E (open squares and dashed grey shading). The central wavelength of the Band 10 measurement for HZ10-C+E is shifted by $+10\mu\text{m}$ for visual clarity. All ALMA bands used in this work are showing through the vertical shading, with those used in the composite image shaded in the same color.

a dust emissivity index of $\beta_{\text{IR}} = 2.2 \pm 0.4$.² The corresponding dust SED peaks at a wavelength of $\lambda_{\text{rest}} = 76^{+7}_{-6}\mu\text{m}$, i.e., between ALMA Bands 8 and 9. Integrating the best-fit MBB across rest-frame 8 – 1000 μm yields a total infrared luminosity of $\log(L_{\text{IR}}/L_{\odot}) = 12.4 \pm 0.1$, which classifies HZ10 as a ULIRG, consistent with previous works (e.g., Faisst et al. 2020). Using the conversion factor from Kennicutt (1998), this yields an obscured star formation rate (SFR) of $\text{SFR}_{\text{IR}} = (1.1 \times 10^{-10}) \times (L_{\text{IR}}/L_{\odot}) = 268^{+66}_{-55} M_{\odot} \text{yr}^{-1}$.³ The total SFR of HZ10, including also the UV-based SFR from Capak et al. (2015), is then $\text{SFR} = 304^{+67}_{-55} M_{\odot} \text{yr}^{-1}$. This suggests that $f_{\text{obs}} = 88^{+2}_{-3}\%$ of its star formation is obscured by dust, in line with the obscured fraction inferred for similarly massive galaxies at lower redshift ($z \lesssim 2.5$; Whitaker et al. 2017), but in excess of what is typically seen in galaxies at $z \approx 4 - 7$ (Fudamoto et al. 2020; Algera et al. 2023).

Given the robust sampling of the dust SED of HZ10 at six distinct wavelengths, it is possible to fit its far-IR emission with more complicated models than an optically thin modified blackbody. We discuss these additional fits in detail in Appendix C, while we summarize the results here. First of all, previous studies of HZ10 have generally assumed its dust emission to be optically thick at wavelengths shorter than $\lambda_{\text{thick}} = 100\mu\text{m}$ (Faisst et al. 2020; Villanueva et al. 2024). In the upper right panel of Fig. C.1, we present a similar fit with λ_{thick} fixed to this value, which yields $T_{\text{dust}} = 51^{+8}_{-7} \text{K}$, fully consistent with that measured in Faisst et al. (2020) and Villanueva et al. (2024). The corresponding dust mass of $\log(M_{\text{dust}}/M_{\odot}) = 7.8 \pm 0.2$ is furthermore consistent with our fiducial fit within the uncertainties.

Leveraging the new Band 10 observations, we can also attempt to constrain the wavelength where the optical depth reaches unity directly. We therefore perform another fit to the far-IR emission of HZ10 (lower left panel in Fig. C.1) with λ_{thick} kept free. However, despite bracketing the peak of the dust SED with the Band 8, 9 and 10 data, the current obser-

vations cannot distinguish between mostly optically thin dust ($\lambda_{\text{thick}} \ll 100\mu\text{m}$) and dust with $\lambda_{\text{thick}} \sim 100 - 150\mu\text{m}$, while only large values of $\lambda_{\text{thick}} \gtrsim 170\mu\text{m}$ can currently be ruled out. While the dust temperature and mass cannot be well constrained in this general-opacity fit, we note that the inferred dust mass of $\log(M_{\text{dust}}/M_{\odot}) = 7.9^{+0.2}_{-0.5}$ remains consistent with our fiducial optically thin value within the uncertainties.

Finally, we consider a multi-temperature dust model. HZ10 is nearly equally luminous in Bands 8, 9 and 10 (Table B.1), which is characteristic of emission from dust at a range of temperatures (e.g., Magnelli et al. 2012a; Casey et al. 2014). Indeed, the spatially resolved analysis of HZ10 in Villanueva et al. (2024), which utilizes the high-resolution ALMA data in Bands 7 and 9, suggests $\Delta T_{\text{dust}} \sim 5 - 10 \text{K}$ differences between the dust temperatures of HZ10-C+E, HZ10-W, and the ‘bridge’ connecting the two. To account for such dust at multiple temperatures, we perform a fit to the ALMA photometry of HZ10 adopting the multi-temperature prescription from Sommovigo & Algera (2025, lower right panel in Fig. C.1). This yields a dust mass of $\log(M_{\text{dust}}/M_{\odot}) = 8.2^{+0.3}_{-0.2}$, which is fully consistent with the value inferred using our fiducial single-temperature model.

As is clear from both the brief above discussion and the more extended one in Appendix C, fitting more elaborate models to the ALMA photometry of HZ10 does not result in a significantly different inferred dust mass. Similarly, the infrared luminosity and dust emissivity index are not strongly dependent on the precise fitting function, while the dust temperature is more strongly affected by assumptions regarding the optical depth (see also da Cunha et al. 2021; Ismail et al. 2023; Algera et al. 2024a; Lower et al. 2024). For general consistency with much of the recent high-redshift literature (e.g., Bakx et al. 2021; Sommovigo et al. 2022; Algera et al. 2024b,a; Valentino et al. 2024), we proceed with our optically thin model as fiducial. Next-generation far-IR missions such as PRIMA (Moulet et al. 2023) will be crucial to better constrain the importance of optically thick and multi-temperature dust at early cosmic epochs.

In what follows, we are mainly interested in the HZ10-C+E system, which Telikova et al. (2024) found can be modeled as a disturbed rotating disk. Given that HZ10 is not resolved in the available Band 4 and 8 observations, we perform an additional fit to just the Band 7, 9 and 10 data. As in our fiducial model for HZ10, we assume a fully optically thin MBB, adopting a narrower Gaussian prior on β_{IR} with a mean (standard deviation)

² We note that, had we assumed a flat prior on β_{IR} between $1 < \beta_{\text{IR}} < 4$ following Algera et al. (2024a), we would recover a slightly steeper but overall consistent value of $\beta_{\text{IR}} = 2.5^{+0.6}_{-0.5}$.

³ We convert the Kennicutt (1998) calibration to the Chabrier IMF assumed in this work by multiplying by 0.63, following Madau & Dickinson (2014).

of 2.2 (0.4) based on the global fit. We show the fit to HZ10-C+E in Figure 2 and present the results in Table 1. Although the Band 10 flux density of HZ10-C+E slightly exceeds our best-fit model, this does not significantly affect the fit owing to the low signal-to-noise ratio of the data. On the other hand, the high S/N of the Band 7 and 9 observations still enable accurate constraints on the dust mass of HZ10-C+E of $\log(M_{\text{dust}}/M_{\odot}) = 7.9 \pm 0.2$.

4. Discussion

4.1. The molecular and atomic gas mass budget in HZ10-C+E

Given the wealth of ancillary data available for HZ10, we can study its mass budget in greater detail than for the large majority of main-sequence star-forming galaxies at $z \gtrsim 4$. We begin by expressing the total mass of HZ10-C+E as:

$$M_{\text{bar}} - M_{\star} - M_{\text{dust}} - M_{\text{HI}} - M_{\text{mol}} = 0, \quad (1)$$

where M_{bar} is the baryonic mass, M_{HI} is the atomic gas mass, and M_{mol} is the molecular gas mass.

We now discuss the values of each mass component listed in Eqs. (1)–(3) for HZ10-C+E. Based on a morpho-kinematic analysis of sensitive, high-angular-resolution ($\approx 0.3''$) [C II] data from the CRISTAL survey (Herrera-Camus et al. 2025), Telikova et al. (2024) find that HZ10-C+E is a rotating disk. Its rotation was modeled using the Python-based forward modeling code DYSMALPY (Davies et al. 2004a,b, 2011; Cresci et al. 2009; Wuyts et al. 2016; Lang et al. 2017; Price et al. 2021; Lee et al. 2025), yielding a low dark-matter fraction of $\approx 30\%$ within the effective radius ($1 \times R_{\text{eff}}$) and a total baryonic mass of $\log(M_{\text{bar}}/M_{\odot}) = 11.1^{+0.2}_{-0.3}$.

For the stellar mass, we have a global mass measurement based on SED modeling using the code CIGALE (Boquien et al. 2019) that corresponds to $\log(M_{\star}/M_{\odot}) = 10.35 \pm 0.37$. The details of the photometric filters and fitting parameters used in the modeling are provided in Mitsunashi et al. (2024, Appendix B). Since *JWST*/NIRCam data is not available for HZ10, we estimate that the stellar mass of HZ10-C+E is approximately 70% of the global value, based on the scaling of the *JWST*/NIRSpec 4 μm continuum flux between the HZ10-C+E and HZ10-W components (Jones et al. 2024, their Fig. 5).

For the atomic gas, the only available tracer is the [C II] line, one of the primary coolants of the cold, neutral ISM (e.g., Wolfire et al. 2022), and thus linked to the atomic gas in galaxies, particularly in their outer regions (e.g., Madden et al. 1993; de Blok et al. 2016). Heintz et al. (2021) provide a calibration of β_{HI} for star-forming galaxies as a function of metallicity based on direct measurements of relative abundances along lines of sight through the ISM of γ -ray burst host galaxies. This method provides an upper limit on the HI gas mass physically associated with the [C II]-emitting region. For the metallicity of HZ10, this calibration yields $\beta_{\text{HI}} \approx 47 M_{\odot}/L_{\odot}$. If we aim to measure a β_{HI} value that is more physically representative of the star-forming disk –within $1 - 1.5 \times R_{\text{eff}}$, where the bulk of the CO and [C II] line emission in HZ10 is detected– we can adopt the mass-to-light ratio $M_{\text{HI}}/L_{[\text{CII}]}$ measured in nearby star-forming galaxies by de Blok et al. (2016). Within one effective radius (R_{eff}), this ratio corresponds to $\beta_{\text{HI}} \approx 20 M_{\odot}/L_{\odot}$, which is a factor of ~ 2 lower than the value reported by Heintz et al. (2021). Only at distances of $\approx 3 \times R_{\text{eff}}$ does β_{HI} in nearby galaxies become comparable to that derived by Heintz et al. (2021), reinforcing the interpretation that the latter calibration represents an upper limit to the total atomic gas content of the system (see also Rowland et al. 2025a).

For the molecular gas, we use the detection of the CO(2-1) line ($S_{\text{CO}(2-1)}\Delta\nu = 0.1 \pm 0.02 \text{ Jy km s}^{-1}$; Pavesi et al. 2019).

There are currently no observational constraints on the molecular gas excitation in normal star-forming galaxies at $z \approx 5$. Therefore, we assume $L'_{\text{CO}(2-1)}/L'_{\text{CO}(1-0)} = 1$, consistent with the values observed in star-forming galaxies at $z \approx 1-2$ (e.g., Aravena et al. 2014; Daddi et al. 2015; Genzel et al. 2015; Tacconi et al. 2020; Boogaard et al. 2020). In both cases, we consider only the [C II] or CO luminosity from HZ10-C+E. For the spatially resolved [C II] observations, measuring the flux from the HZ10-C+E component is straightforward, as this region is spatially resolved and accounts for $\sim 60\%$ of the total flux ($S_{[\text{CII}]}^{\text{total}}\Delta\nu = 4.9 \pm 0.02 \text{ Jy km s}^{-1}$; Telikova et al. 2024). However, for the CO(2-1) line, only a global measurement is available (Pavesi et al. 2019). By analogy with the [C II] case, we therefore assume that $\sim 60\%$ of the total CO(2-1) emission originates from the HZ10-C+E component.

For the CO-to-H₂ conversion factor, we consider four values: (1) a Milky Way (MW)-based value ($\alpha_{\text{CO}} = 4.3 M_{\odot} (\text{K km s}^{-1})^{-1}$; e.g., Bolatto et al. 2013); (2) the typical value assumed for nearby ULIRGs and merger-driven starbursts ($\alpha_{\text{CO}} = 1 M_{\odot} (\text{K km s}^{-1})^{-1}$; e.g., Downes & Solomon 1998; Tacconi et al. 2008); (3) the $\alpha_{\text{CO}} = 1.5 M_{\odot} (\text{K km s}^{-1})^{-1}$ obtained for a $z = 6$ Lyman-break galaxy from the SERRA simulations with a metallicity similar to that of HZ10 (Vallini et al. 2018); and (4-5) two estimates specific to HZ10-C+E: $\alpha_{\text{CO}} = 3.9 M_{\odot} (\text{K km s}^{-1})^{-1}$, derived from its dust temperature following the calibration by Magnelli et al. (2012b), and $\alpha_{\text{CO}} = 4.9 M_{\odot} (\text{K km s}^{-1})^{-1}$, estimated from its metallicity following Bolatto et al. (2013).

Alternatively to CO, we can use the [C II] luminosity as a tracer of the molecular gas. For the [C II]-to-H₂ conversion factor, we adopt three calibrations: (1) the calibration by Zanella et al. (2018), based on (U)LIRGs and main-sequence star-forming galaxies up to $z \sim 2$; (2) the calibration by Madden et al. (2020), derived from local dwarf galaxies; and (3) the calibration by Rizzo et al. (2021), based on the dynamical properties of 5 dusty star-forming galaxies at $z \approx 4.5$, of which 4 lie above the main-sequence of star-forming galaxies, as opposed to HZ10.

Figure 3 shows the total mass budget of HZ10 as a function of α_{CO} (left panel), $\alpha_{[\text{CII}]}$ (right panel), and β_{HI} . The blue line represents the solution to Equation 1, while the red shading indicates the forbidden region where $M_{\text{bar}} < M_{\star} + M_{\text{dust}} + M_{\text{mol}} + M_{\text{HI}}$. In both panels, the values of β_{HI} from Heintz et al. (2021), derived using the metallicity of HZ10, and from the inner $\sim 1 \times R_{\text{eff}}$ of nearby galaxies (de Blok et al. 2016) are shown as green horizontal lines.

We begin by discussing the left panel, where the molecular gas mass is derived from the CO line emission. The α_{CO} conversion factors inferred from the dust temperature and metallicity of HZ10-C+E are both comparable to the Milky Way-like value of α_{CO} . Adopting this conversion factor yields a molecular gas mass of $M_{\text{mol}} \approx 6.0 \times 10^{10} M_{\odot}$ and a molecular gas fraction, defined as $\mu_{\text{mol}} = M_{\text{mol}}/M_{\star}$, of $\mu_{\text{mol}} \approx 3.8$, which is probably too gas rich compared to the expectations for star-forming galaxies at this redshift. If instead we assume the α_{CO} value typical of (U)LIRGs, the inferred molecular gas fraction decreases by a factor $\alpha_{\text{CO}}/\alpha_{\text{ULIRG}} = 4.3/1$, that is, to $\mu_{\text{mol}} \approx 0.9$. This value is more in line with the expectations from scaling relations of galaxies between $0 \lesssim z \lesssim 4$ (e.g., Tacconi et al. 2020). Interestingly, a similarly low α_{CO} value has been reported by Vallini et al. (2018) for a high-redshift star-forming galaxy drawn from the SERRA simulations, with a metallicity comparable to that of HZ10. In particular, Vallini et al. (2018) found $\alpha_{\text{CO}} \approx 1.5$, attributing this lower value to the combination of strong turbulence, high gas densities, and the elevated CMB temperature at early cosmic times.

It is moreover important to note that when a Milky Way-based (or similar) α_{CO} is adopted, the resulting mass budget leaves no room for the atomic gas mass estimated using the

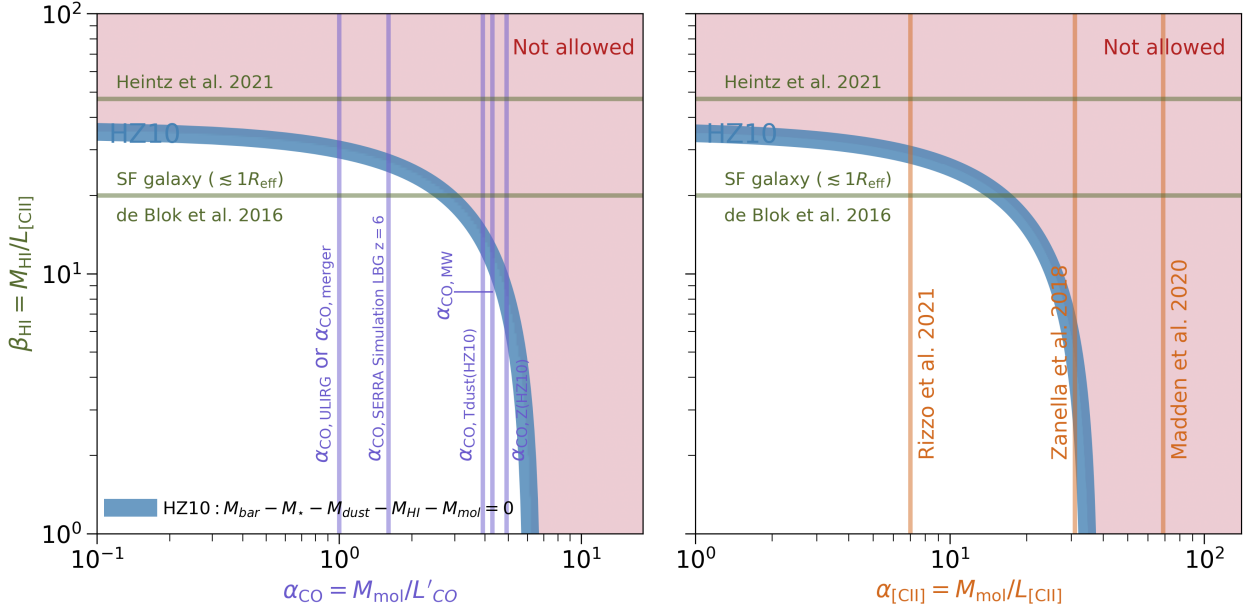


Fig. 3. (Left) Total mass budget of HZ10 as a function of the CO-to-H₂ (α_{CO}) and [CII]-to-HI (β_{HI}) conversion factors. The blue line represents the case where $M_{\text{bar}} - M_{\star} - M_{\text{dust}} - M_{\text{HI}} - M_{\text{mol}} = 0$. The shaded regions indicate the forbidden region where this expression is less than zero. The green and red lines correspond to typical values of β_{HI} and α_{CO} , respectively, commonly assumed in the literature for different galaxy conditions. For the molecular gas, these include: MW-like α_{CO} (e.g., Bolatto et al. 2013), ULIRG-like or merger-like α_{CO} (e.g., Downes & Solomon 1998; Tacconi et al. 2008), α_{CO} from a SERRA simulated Lyman-break galaxy at $z = 6$ (Vallini et al. 2018), and α_{CO} based on the dust temperature and metallicity of HZ10-C+E following Magnelli et al. (2012b) and Bolatto et al. (2013), respectively. For the atomic hydrogen gas, we include the calibration by Heintz et al. (2021) and the mass-to-light ratio observed within one effective radius in nearby star-forming galaxies (de Blok et al. 2016). (Right) Similar to the left panel, but here the x-axis represents the [CII]-to-H₂ ($\alpha_{\text{[CII]}}$) conversion factor. The $\alpha_{\text{[CII]}}$ calibrations by Zanella et al. (2018), Madden et al. (2020), and Rizzo et al. (2021) are included.

calibration by Heintz et al. (2021), as the intersection of the corresponding lines lies within the forbidden region. Conversely, the only scenario in which the CO-based molecular gas and the HI mass are consistent with the total mass budget of HZ10 is when the [CII]-to- M_{HI} calibration factor based on the inner R_{eff} radius of nearby galaxies, $\beta_{\text{HI}} \approx 20 M_{\odot}/L_{\odot}$, is adopted.

We continue our analysis, this time considering the [CII]-based molecular gas mass estimates (right panel of Fig. 3). Using the calibration by Rizzo et al. (2021), we derive a molecular gas mass of $M_{\text{mol}} = 1.7 \times 10^{10} M_{\odot}$ and a corresponding molecular gas fraction of $\mu_{\text{mol}} = 0.5$. The other three [CII]-to-H₂ calibrations yield systematically higher molecular gas masses: the Zanella et al. (2018) and Madden et al. (2020) relations give values larger by factors of ≈ 4 and ≈ 10 , respectively.

Similar to the case of the CO-based molecular gas estimates, and considering the associated uncertainties, in the case of HZ10-C+E only the calibration by Rizzo et al. (2021) can be used together with the HI mass calibration by Heintz et al. (2021) without exceeding the total dynamical mass of the system. Conversely, the calibration by Zanella et al. (2018) is consistent only when adopting the [CII]-to- M_{HI} conversion factor derived for the inner R_{eff} of nearby galaxies. Finally, the calibration by Madden et al. (2020), based on a sample of low-metallicity dwarf galaxies, significantly overpredicts the molecular gas mass relative to the other [CII]- and CO-based tracers. This is expected, as the ISM conditions in low-metallicity dwarfs most likely differ from those in massive, dusty, star-forming galaxies at high redshift such as HZ10.

All in all, this simple analysis shows the difficulties of simultaneously measuring the HI and H₂ masses from [CII] line emission, given the varied nature of the calibrations and the fact that [CII] emission is multi-phase, arising from both molecular and atomic gas. A more practical and physically motivated approach moving forward may be to use the [CII] line as a tracer of

the total cold gas – that is, the combined molecular and atomic components of the ISM. This is analogous to the approach commonly adopted when using the dust continuum as a gas tracer, since dust is mixed with both the molecular and atomic phases of the ISM (e.g., Scoville et al. 2017). This perspective has also been followed in recent studies, such as the SERRA simulations by Vallini et al. (2025), which derived scaling relations between M_{gas} and the [CII] line luminosity that depend on both the metallicity and the size of the system. Following this approach, in the case of HZ10, the [CII] conversion factor between the total cold gas mass ($M_{\text{ISM}} = M_{\text{HI}} + M_{\text{mol}} = M_{\text{bar}} - M_{\star} - M_{\text{dust}}$) and the [CII] luminosity is $\alpha_{\text{[CII]}}^{\text{ISM}} = 39_{-25}^{+50} M_{\odot}/L_{\odot}$.

One clear outcome of this analysis –independent of the uncertainties in the baryonic and stellar mass estimates and in the adopted calibration factors– is that HZ10 is a galaxy rich in cold ISM gas, with a cold gas-to-stellar mass fraction of ≈ 2 . This high value is consistent with the [CII]-based measurements for star-forming galaxies at $4 \lesssim z \lesssim 7$ reported by Dessauges-Zavadsky et al. (2020) and Aravena et al. (2024), as well as with the extrapolation of the scaling relation derived by Tacconi et al. (2018, 2020) for star-forming galaxies at $z \lesssim 4$, and with the SERRA simulated galaxies presented by Vallini et al. (2025).

The original SERRA relation for $\log \alpha_{\text{[CII]}}$ versus metallicity (see Eq. 1 in Vallini et al. 2025) was calibrated using metallicities averaged over a $5 \times 5 \text{ kpc}^2$ region around each simulated galaxy. This makes it not directly comparable to our derivation for HZ10. To address this, we recomputed the relation using the metallicity averaged within the [CII] half-light radius of the simulated galaxies, ensuring a more consistent spatial comparison (Vallini et al. in preparation). This yields a relation of

$$\log \alpha_{\text{[CII]}} = -0.38 \log(Z/Z_{\odot}) + 1.12,$$

which corresponds to $\alpha_{\text{[CII]}} \approx 16$ for HZ10-C+E. This value is consistent, within the uncertainties, with the dynamically inferred value.

4.2. The dust-to-gas and dust-to-metal ratios of HZ10 and HZ10-C+E

Given that our ALMA observations both bracket the peak of the dust SED and cover the Rayleigh-Jeans tail, we obtain robust constraints on the total dust mass of HZ10 of $\log(M_{\text{dust}}/M_{\odot}) = 8.0 \pm 0.1$ given our fiducial optically thin model. We also constrain its dust emissivity index to be $\beta_{\text{IR}} = 2.2 \pm 0.4$, which is consistent with what is typically seen in galaxies at Cosmic Noon (da Cunha et al. 2021; Liao et al. 2024; Bendo et al. 2025) as well as at higher redshifts (Witstok et al. 2023; Algera et al. 2024a).

Using the dust mass obtained from our SED-fitting and the stellar mass from Mitsuhashi et al. (2024), we infer a dust-to-stellar mass ratio of $\log(M_{\text{dust}}/M_{\star}) = -2.31 \pm 0.39$ for HZ10, equivalent to $M_{\text{dust}}/M_{\star} = 5^{+7}_{-3} \times 10^{-3}$. This value is consistent with typical dust-to-stellar mass ratios of $z \approx 4 - 8$ star-forming galaxies (Bakx et al. 2021; Sommovigo et al. 2022; Witstok et al. 2023; Algera et al. 2024a, 2025; Sawant et al. 2025). Assuming a Chabrier (2003) IMF and the Michałowski (2015) framework, the measured ratio for HZ10 corresponds to an IMF-averaged supernova dust yield of $y_{\text{SN}} = 0.41^{+0.60}_{-0.24} M_{\odot}/\text{SN}$. This is in line with the large range of values suggested for SNe ranging from $y_{\text{SN}} < 10^{-3} M_{\odot}$ to $y_{\text{SN}} \sim 1 M_{\odot}$, as recently compiled by Schneider & Maiolino (2024).

However, converting the dust-to-stellar mass ratio to a SN dust yield implicitly assumes negligible contribution from ISM dust growth and AGB stars, which even at high redshift is not necessarily the case (e.g., Leńiewska & Michałowski 2019; Algera et al. 2024a, 2025). To better understand the pathways of dust build-up in HZ10, we shift our focus to HZ10-C+E, where we can leverage the kinematic constraints on its baryonic mass. As in the previous section, we determine the total (atomic + molecular) gas mass of HZ10+C-E as $M_{\text{gas}} = M_{\text{mol}} + M_{\text{HI}} = M_{\text{bar}} - M_{\star} - M_{\text{dust}}$. Using this gas mass, we compute the dust-to-gas ratio $\text{DtG} = M_{\text{dust}}/M_{\text{gas}}$ and – combined with the metallicity of $Z \sim 0.6 Z_{\odot}$ from Jones et al. (2024) – the dust-to-metal ratio $\text{DtM} = \text{DtG}/Z$.

We infer $\log(\text{DtG}) = -3.08^{+0.40}_{-0.33}$ and $\log(\text{DtM}) = -1.00^{+0.41}_{-0.34}$ for HZ10-C+E, and show its DtG and DtM as a function of metallicity in Fig. 4. To place HZ10+C-E in context, we compare to a variety of studies spanning $z \approx 0 - 8$. First of all, we compare to several scaling relations between DtG, DtM and metallicity derived for local galaxies, adopting the best-fit trends from Rémy-Ruyer et al. (2014); De Vis et al. (2019) and Galiano et al. (2021). These works typically infer dust masses from detections in various *Herschel* bands, while gas masses include both molecular and atomic hydrogen.

At slightly higher redshift ($z \approx 1.5 - 2.5$), we compare to the works by Shapley et al. (2020) and Popping et al. (2023). Both studies combine Keck/MOSFIRE rest-optical spectra with ALMA-based dust and gas masses, the latter obtained from low- and mid- J CO lines. As such, these works do not explicitly account for atomic hydrogen, and their DtG and DtM ratios can therefore be considered upper limits. Shapley et al. (2020) adopt a fixed $\alpha_{\text{CO}} = 3.6 M_{\odot} (\text{K km s}^{-1})^{-1}$, while Popping et al. (2023) use the metallicity-dependent prescription from Accurso et al. (2017), which ranges from $\alpha_{\text{CO}} \sim 2.7 - 8.1 M_{\odot} (\text{K km s}^{-1})^{-1}$ for their sample. The dust mass estimates in both works are based on the assumption of a fixed dust temperature of $T_{\text{dust}} \sim 25 - 35 \text{ K}$. We scale their dust masses to the same dust model adopted here (i.e., the κ_{850} from Dunne et al. 2000; Section 3), which reduces the Shapley et al. (2020) and Popping et al. (2023) dust masses by 0.19 and 0.32 dex, respectively.

At higher redshifts ($z \approx 6 - 8$), we compare to Algera et al. (2025), who recently compiled the dust-to-gas and dust-to-metal ratios of 15 galaxies with ALMA [C II] $158 \mu\text{m}$ observations, predominantly taken from the REBELS-IFU survey (Bouwens et al. 2022; Rowland et al. 2025b). Algera et al. (2025) adopt the Zanella et al. (2018) conversion to infer the gas masses of their sample, which they argue accounts for both molecular and atomic gas (see also Dessauges-Zavadsky et al. 2020; Aravena et al. 2024). This moreover agrees with our analysis in Section 4.1, where applying the Zanella et al. [C II]-to- M_{mol} conversion factor indeed leaves little room for atomic gas in HZ10-C+E. To match our dust model, we scale the Algera et al. (2025) dust masses downwards by 0.33 dex.

We also compare to the $z = 7.31$ galaxy REBELS-25, which Rowland et al. (2024) recently demonstrated to be a dynamically cold disk based on high-resolution [C II] observations. Leveraging their dynamical mass measurement, as well as the stellar mass reported in Rowland et al. (2025b) and the dust mass inferred by Algera et al. (2024a), we infer the total gas mass of REBELS-25 in the same way as for HZ10-C+E in Section 4.1. Given that Rowland et al. (2025b) quote only the dynamical mass of REBELS-25, we adopt a dark matter fraction of 30 % – the same as inferred for HZ10-C+E by Telikova et al. (2024) – to convert this to a baryonic mass. We moreover adopt its metallicity to be $12 + \log(\text{O}/\text{H}) = 8.62 \pm 0.17$ as inferred by Rowland et al. (2025b).

Finally, we compare to three model tracks from the semi-analytical models by Popping et al. (2017), Vijayan et al. (2019) and Mauerhofer et al. (2025), evaluated at $z \approx 6$. These models include both dust production and destruction processes, albeit with different efficiencies. Among the three, the Popping et al. (2017) models predict the largest dust enrichment by $z \approx 6$, with the DtG ratios approaching those observed in local galaxies. In their fiducial model, dust production takes place primarily through growth in the ISM, which is predicted to be particularly efficient for massive and metal-rich galaxies such as HZ10.

The Vijayan et al. (2019) models similarly predict that ISM growth is the dominant dust production mechanism in galaxies at $z \approx 6$, although it proceeds at a lower rate than in the models by Popping et al. (2017). As a result, the DtG and DtM ratios predicted by the Vijayan et al. (2019) models are ~ 1 dex lower than those by Popping et al. (2017) at high metallicities ($12 + \log(\text{O}/\text{H}) \gtrsim 8.2$). Furthermore, due to this delayed grain growth, the Vijayan et al. (2019) models predict a more or less flat trend between dust-to-metal ratio and metallicity at $z \approx 6$, while only by $z \lesssim 3$, the DtM ratio starts to consistently increase for more metal-rich galaxies.

Finally, we compare to the recent semi-analytical models by Mauerhofer et al. (2025), which build upon the dust production and destruction framework from Dayal et al. (2022). In their models, dust production is predominantly due to supernovae, which are assigned a fixed dust yield of $y_{\text{SN}} = 0.5 M_{\odot}$. This results in a linear scaling between DtG ratio and metallicity, while the dust-to-metal ratio is independent of metallicity. While the Mauerhofer et al. (2025) models are able to produce massive galaxies by $z \approx 6$ (up to $M_{\star} \sim 10^{11.5} M_{\odot}$), they are predicted to, on average, have relatively low metallicities ($Z \lesssim 0.2 Z_{\odot}$). Consequently, the Mauerhofer et al. (2025) models do not extend beyond $Z \gtrsim 0.5 Z_{\odot}$ by $z \approx 6$, slightly below the metallicity of HZ10. Nevertheless, owing to the high SN dust yields implemented in their models, Mauerhofer et al. (2025) predict the highest DtG and DtM ratios at a fixed metallicity among the three models we compare to.

Overall, we find that the DtG and DtM ratios of HZ10-C+E fall $\sim 0.5 - 1$ dex below the local scaling relations. Given its high metallicity ($Z \sim 0.6 Z_{\odot}$; Jones et al. 2024), HZ10 is expected to lie in the regime where ISM dust growth is efficient ($Z \gtrsim 0.2 Z_{\odot}$; e.g., Asano et al. 2013; Choban et al. 2024). The

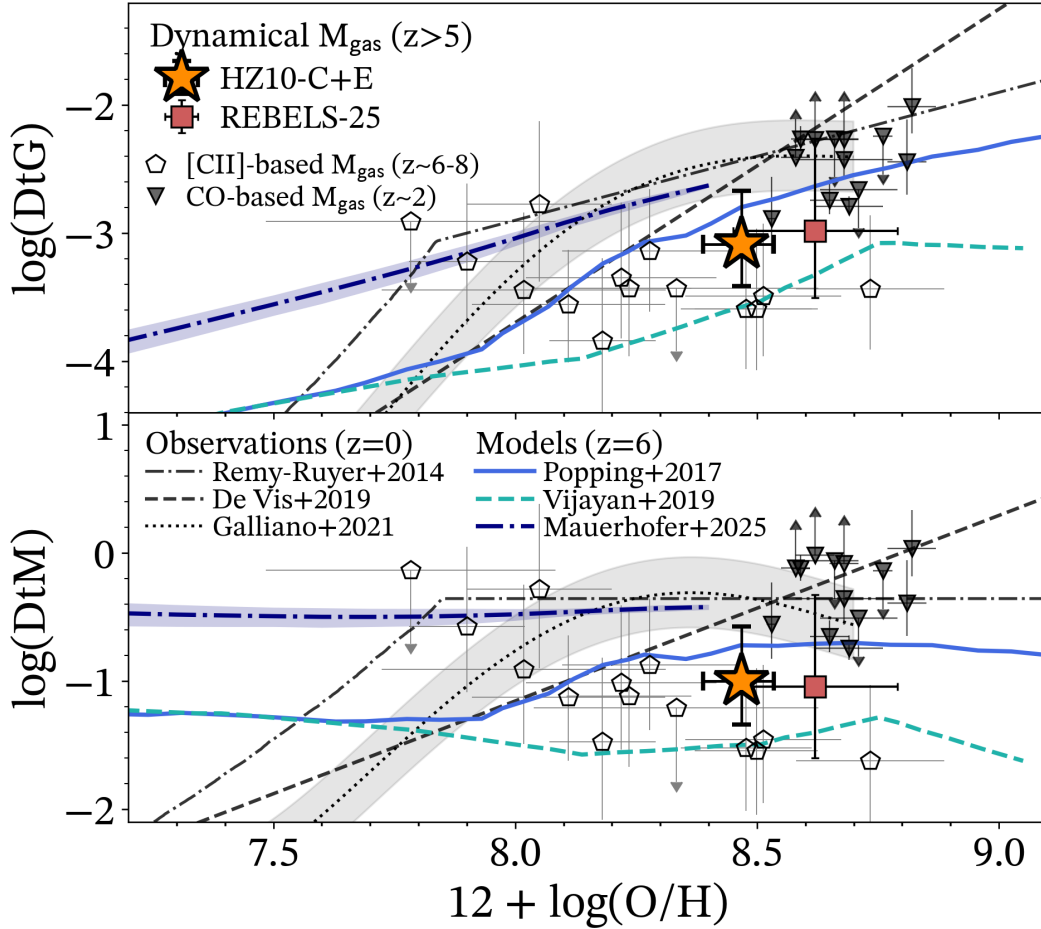


Fig. 4. The dust-to-gas (DtG; *upper panel*) and dust-to-metal (DtM; *bottom panel*) ratios of HZ10-C+E (orange star) as a function of metallicity. For the dust mass, we use our fiducial optically thin model, while the gas mass of HZ10-C+E is determined as the difference of its baryonic mass – inferred through kinematic modeling by [Telikova et al. \(2024\)](#) – and stellar mass ([Mitsuhashi et al. 2024](#)). The metallicity of HZ10-C+E was recently inferred through *JWST*/NIRSpec IFU observations by [Jones et al. \(2024\)](#). We compare to a similar dynamically-inferred DtG and DtM for the $z = 7.31$ galaxy REBELS-25 (red square; [Rowland et al. 2024, 2025b; Algera et al. 2025](#)), while at Cosmic Noon we leverage ALMA-based dust and gas mass measurements from [Shapley et al. \(2020\)](#) and [Popping et al. \(2023, black triangles\)](#). The open pentagons represent [C II]-based measurements from [Algera et al. \(2025\)](#). Finally, we overlay several local relations ([R  my-Ruyer et al. 2014; De Vis et al. 2019; Galliano et al. 2021](#), grey lines) as well as model tracks at $z \approx 6$ ([Popping et al. 2017; Vijayan et al. 2019; Mauerhofer et al. 2025](#), colored lines). Despite its metal-enriched nature, we find that HZ10-C+E falls below the local scaling relations, suggesting either a limited efficiency of ISM dust growth in HZ10, or efficient dust destruction.

lower DtG and DtM ratios may therefore suggest that HZ10 has not yet efficiently formed dust through ISM dust growth, indicating this process operates on a longer characteristic timescale. Alternatively, given that HZ10 is undergoing a powerful starburst, it is possible that the resulting supernovae are able to efficiently destroy dust within the galaxy through shattering and sputtering, or eject it from the galaxy through outflows.

The other high-redshift galaxy with dynamical constraints on its total gas mass and multi-band constraints on M_{dust} , REBELS-25, shows a similar DtG and DtM ratio to HZ10-C+E. Unlike HZ10, REBELS-25 does not appear to be undergoing a merger ([Rowland et al. 2024](#)), and it has a $\sim 3\times$ lower star formation rate than HZ10 ([Algera et al. 2024a](#)). Both galaxies show a typical DtM ratio of $\log(\text{DtM}) \approx -1$, which is consistent with the values obtained for $z \sim 6-8$ galaxies by [Algera et al. \(2025\)](#) leveraging [C II]-based gas masses, but lower than what is seen in galaxies in the nearby Universe.

The measured DtG and DtM ratios of HZ10-C+E place it in between the model tracks from [Popping et al. \(2017\)](#) and [Vijayan et al. \(2019\)](#), which we recall ascribe most of dust production at $z \approx 6$ to growth in the ISM. Consequently, this would suggest

that grain growth is already moderately efficient at $z \approx 6$. We caution, however, that [Popping et al. \(2017\)](#) also explore a variety of alternative dust production models in their work, and demonstrate that efficient SN dust production can also lead to similar DtG and DtM ratios as in their fiducial model shown in Figure 4. Distinguishing between these scenarios requires a significantly larger sample of high-redshift galaxies with robust dust and gas mass measurements – especially at the metal-poor end where models relying on ISM dust growth predict lower DtG ratios. Given the intrinsic faintness of such metal-poor and therefore typically low-mass galaxies, exploiting gravitational lensing provides a promising pathway of studying dust build-up in such systems (c.f., [Heintz et al. 2023, 2025; Valentino et al. 2024](#)).

We find that the dust-to-gas and dust-to-metal ratios of both HZ10-C+E and REBELS-25 are inconsistent with those predicted by the [Mauerhofer et al. \(2025\)](#) models, which exceed the measurements by ~ 0.5 dex. This is particularly interesting given that [Mauerhofer et al. \(2025\)](#) demonstrate that their modeled dust-to-stellar mass ratios match those observed in high-redshift galaxies from ALPINE ([Fudamoto et al. 2020](#)) and REBELS ([Bouwens et al. 2022; Inami et al. 2022](#)). In turn, it is impera-

tive to explore a wider range of scaling relations – beyond the typical comparison of dust and stellar masses (e.g., [Leśniewska & Michałowski 2019](#); [Witstok et al. 2023](#); [Algera et al. 2024b](#)) – to more clearly distinguish between various models of dust build-up.

5. Conclusions

In this paper, we have studied the ISM properties of the $z = 5.65$ main-sequence, star-forming galaxy HZ10 in detail. In particular, we focus on the key question of how much gas (atomic and molecular) and dust is present in its ISM. To address this, we combine ALMA dust continuum observations ([Faisst et al. 2020](#); [Villanueva et al. 2024](#)) including new Band 10 and 4 observations, detailed kinematics from [C II] line observations ([Telikova et al. 2024](#)), *JWST*/NIRSpec measurements of the metallicity ([Jones et al. 2024](#)), and JVL A observations of the molecular gas via the CO(2-1) transition ([Pavesi et al. 2019](#)). Our main results can be summarized as follows:

1. We detect the dust continuum emission in ALMA Bands 10 and 4, probing the peak and Rayleigh–Jeans tail of the dust SED, respectively. Combined with ancillary ALMA data ([Faisst et al. 2020](#); [Villanueva et al. 2024](#)), this allows us to cover the dust SED from $\lambda_{\text{rest}} \approx 50\text{--}300\ \mu\text{m}$, providing the most complete rest-frame IR SED for a normal star-forming galaxy at this redshift.
2. Fitting the global dust SED of HZ10 with a single-temperature modified blackbody and assuming optically thin emission, we infer a dust mass of $\log(M_{\text{dust}}/M_{\odot}) = 8.0 \pm 0.1$, a dust temperature of $T_{\text{dust}} = 37^{+6}_{-5}\ \text{K}$, and a dust emissivity index of $\beta_{\text{IR}} = 2.2 \pm 0.4$. This corresponds to a total infrared luminosity of $\log(L_{\text{IR}}/L_{\odot}) = 12.4 \pm 0.1$, and a total (UV+IR) star formation rate of $\text{SFR} = 304^{+67}_{-55}\ M_{\odot}\ \text{yr}^{-1}$. We infer consistent values when fitting more sophisticated dust models to the ALMA data.

We proceed by focusing on HZ10-C+E, the rotationally-supported component of the HZ10 system ([Telikova et al. 2024](#)) for which we can infer the total ISM mass based on its [C II] kinematics. Our results can be summarized as follows:

3. Regarding the independent calibrations of the molecular and atomic gas masses based on the [C II] line emission reported in the literature, we find that, within the uncertainties, the total gas mass is compatible with the total mass budget from the kinematic modeling only if: (1) the β_{HI} calibration by [Heintz et al. \(2021\)](#) is combined with a typical α_{CO} for (U)LIRGs or with the $\alpha_{\text{[CII]}}$ values from [Rizzo et al. \(2021\)](#); or (2) the β_{HI} value found within $1\ R_{\text{eff}}$ in nearby galaxies by [de Blok et al. \(2016\)](#) is combined with either the Milky Way α_{CO} or the $\alpha_{\text{[CII]}}$ calibration from [Zanella et al. \(2018\)](#). In this sense, because we do not know a priori what fraction of the [C II] emission in high-redshift galaxies arises from the molecular or the atomic phase, it is preferable to adopt a calibration factor that directly targets the total (atomic + molecular) gas mass, as also advocated by the SERRA simulation work of [Vallini et al. \(2025\)](#). For HZ10-C+E, we find that the [C II]-to- M_{ISM} conversion factor corresponds to $\alpha_{\text{[CII]}}^{\text{ISM}} = 39^{+50}_{-25}\ M_{\odot}\ L_{\odot}^{-1}$.
4. Combining the total gas mass obtained from the [C II] kinematics of HZ10-C+E with the dust mass from SED fitting ($\log(M_{\text{dust}}/M_{\odot}) = 7.9 \pm 0.2$), we study its dust production pathways through the dust-to-gas ($\log \text{DtG} = -3.08^{+0.40}_{-0.33}$) and dust-to-metal ($\log \text{DtM} = -1.00^{+0.41}_{-0.34}$) ratios. We find that HZ10-C+E falls below the local scaling relations of DtG and

DtM with metallicity, suggesting less efficient dust production or enhanced dust destruction compared to local galaxies. Aided by a comparison to theoretical models at $z \approx 6$, we speculate the lower dust contents are due to inefficient grain growth in its ISM, despite the relatively metal-enriched nature of HZ10-C+E ($Z \approx 0.6\ Z_{\odot}$; [Jones et al. 2024](#)).

Using HZ10 as a case study, we have demonstrated how synergistic observations from some of the world’s most advanced telescopes (*JWST*, ALMA, JVL A) can be used to unravel the detailed baryonic mass budget of high-redshift galaxies. In the future, similar observations of larger galaxy samples will be able to robustly constrain the various conversion factors between emission line luminosities and molecular/atomic gas masses (i.e., α_{CO} , $\alpha_{\text{[CII]}}$, β_{HI}), as well as constrain their dust contents through multi-band far-IR continuum sampling. Combined, such observations will provide the most detailed possible insights into the ISM contents and evolutionary pathways of the distant galaxy population.

Acknowledgements. H.S.B.A gratefully acknowledges support from Academia Sinica through grant AS-PD-1141-M01-2. R.H.-C. thanks the Max Planck Society for support under the Partner Group project “The Baryon Cycle in Galaxies” between the Max Planck for Extraterrestrial Physics and the Universidad de Concepción. R.H.-C. also gratefully acknowledges financial support from ANID - MILENIO - NCN2024_112 and ANID BASAL FB210003. M.A. is supported by FONDECYT grant number 1252054, and gratefully acknowledges support from ANID Basal Project FB210003 and ANID MILENIO NCN2024_112. E.d.C. acknowledges support from the Australian Research Council (projects DP240100589). P.D. warmly acknowledges support from an NSERC discovery grant (RGPIN-2025-06182). G.C.J. acknowledges support by the Science and Technology Facilities Council (STFC), by the ERC through Advanced Grant 695671 “QUENCH”, and by the UKRI Frontier Research grant RISEandFALL.

References

- Accurso, G., Saintonge, A., Catinella, B., et al. 2017, *MNRAS*, 470, 4750
 Algera, H. S. B., Inami, H., De Looze, I., et al. 2024a, *MNRAS*, 533, 3098
 Algera, H. S. B., Inami, H., Oesch, P. A., et al. 2023, *MNRAS*, 518, 6142
 Algera, H. S. B., Inami, H., Sommovigo, L., et al. 2024b, *MNRAS*, 527, 6867
 Algera, H. S. B., Rowland, L., Stefanon, M., et al. 2025, *MNRAS*[arXiv:2501.10508]
 Aravena, M., Heintz, K., Dessauges-Zavadsky, M., et al. 2024, *A&A*, 682, A24
 Aravena, M., Hodge, J. A., Wagg, J., et al. 2014, *MNRAS*, 442, 558
 Asano, R. S., Takeuchi, T. T., Hirashita, H., & Nozawa, T. 2013, *MNRAS*, 432, 637
 Bakx, T. J. L. C., Sommovigo, L., Carniani, S., et al. 2021, *MNRAS*, 508, L58
 Bakx, T. J. L. C., Sommovigo, L., Tamura, Y., et al. 2025, arXiv e-prints, arXiv:2511.08327
 Bendo, G. J., Bakx, T. J. L. C., Algera, H. S. B., et al. 2025, *MNRAS*, 540, 1560
 Bolatto, A. D., Wolfire, M., & Leroy, A. K. 2013, *ARA&A*, 51, 207
 Boogaard, L. A., van der Werf, P., Weiss, A., et al. 2020, *ApJ*, 902, 109
 Boquien, M., Burgarella, D., Roehlly, Y., et al. 2019, *A&A*, 622, A103
 Bouwens, R. J., Smit, R., Schouws, S., et al. 2022, *ApJ*, 931, 160
 Burgarella, D., Buat, V., Theulé, P., et al. 2025, arXiv e-prints, arXiv:2504.13118
 Capak, P. L., Carilli, C., Jones, G., et al. 2015, *Nature*, 522, 455
 CASA Team, Bean, B., Bhatnagar, S., et al. 2022, *PASP*, 134, 114501
 Casavecchia, B., Maio, U., Péroux, C., & Ciardi, B. 2025, *A&A*, 693, A119
 Casey, C. M., Narayanan, D., & Cooray, A. 2014, *Phys. Rep.*, 541, 45
 Chabrier, G. 2003, *PASP*, 115, 763
 Chiang, I.-D., Sandstrom, K. M., Chasteney, J., et al. 2024, *ApJ*, 964, 18
 Choban, C. R., Kereš, D., Sandstrom, K. M., et al. 2024, *MNRAS*, 529, 2356
 Ciesla, L., Adscheid, S., Magnelli, B., et al. 2024, arXiv e-prints, arXiv:2412.02557
 Cresci, G., Hicks, E. K. S., Genzel, R., et al. 2009, *ApJ*, 697, 115
 Croxall, K. V., Smith, J. D., Pellegrini, E., et al. 2017, *ApJ*, 845, 96
 da Cunha, E., Groves, B., Walter, F., et al. 2013, *ApJ*, 766, 13
 da Cunha, E., Hodge, J. A., Casey, C. M., et al. 2021, *ApJ*, 919, 30
 Daddi, E., Dannerbauer, H., Liu, D., et al. 2015, *A&A*, 577, A46
 Davies, R., Förster Schreiber, N. M., Cresci, G., et al. 2011, *ApJ*, 741, 69
 Davies, R. I., Tacconi, L. J., & Genzel, R. 2004a, *ApJ*, 613, 781
 Davies, R. I., Tacconi, L. J., & Genzel, R. 2004b, *ApJ*, 602, 148
 Dayal, P., Ferrara, A., Sommovigo, L., et al. 2022, *MNRAS*, 512, 989
 de Blok, W. J. G., Walter, F., Smith, J. D. T., et al. 2016, *AJ*, 152, 51
 De Looze, I., Lamperti, I., Saintonge, A., et al. 2020, *MNRAS*, 496, 3668
 De Vis, P., Jones, A., Viaene, S., et al. 2019, *A&A*, 623, A5
 Dessauges-Zavadsky, M., Ginolfi, M., Pozzi, F., et al. 2020, *A&A*, 643, A5
 Díaz-Santos, T., Armus, L., Charmandaris, V., et al. 2017, *ApJ*, 846, 32
 D’Odorico, V., Feruglio, C., Ferrara, A., et al. 2018, *ApJ*, 863, L29

- Downes, D. & Solomon, P. M. 1998, *ApJ*, 507, 615
- Dunne, L., Eales, S., Edmunds, M., et al. 2000, *MNRAS*, 315, 115
- Faisst, A. L., Fudamoto, Y., Oesch, P. A., et al. 2020, *MNRAS*, 498, 4192
- Feldmann, R. 2015, *MNRAS*, 449, 3274
- Fernández, X., Gim, H. B., van Gorkom, J. H., et al. 2016, *ApJ*, 824, L1
- Fernández Aranda, R., Díaz Santos, T., Hatziminaoglou, E., et al. 2025, *arXiv e-prints*, [arXiv:2502.10503](#)
- Ferrara, A., Pallottini, A., & Sommovigo, L. 2025, *A&A*, 694, A286
- Ferrara, A., Viti, S., & Ceccarelli, C. 2016, *MNRAS*, 463, L112
- Fisher, D. B., Bolatto, A. D., Herrera-Camus, R., et al. 2014, *Nature*, 505, 186
- Frias Castillo, M., Rybak, M., Hodge, J. A., et al. 2024, *arXiv e-prints*, [arXiv:2404.05596](#)
- Fudamoto, Y., Oesch, P. A., Faisst, A., et al. 2020, *A&A*, 643, A4
- Galliano, F., Galametz, M., & Jones, A. P. 2018, *ARA&A*, 56, 673
- Galliano, F., Nersesian, A., Bianchi, S., et al. 2021, *A&A*, 649, A18
- Genzel, R., Tacconi, L. J., Lutz, D., et al. 2015, *ApJ*, 800, 20
- Gurman, A., Hu, C.-Y., Sternberg, A., & van Dishoeck, E. F. 2024, *ApJ*, 965, 179
- Heintz, K. E., Giménez-Arteaga, C., Fujimoto, S., et al. 2023, *ApJ*, 944, L30
- Heintz, K. E., Watson, D., Oesch, P. A., Narayanan, D., & Madden, S. C. 2021, *ApJ*, 922, 147
- Heintz, K. E., Watson, D., Valentino, F., et al. 2025, *arXiv e-prints*, [arXiv:2510.07936](#)
- Herrera-Camus, R., González-López, J., Förster Schreiber, N., et al. 2025, *arXiv e-prints*, [arXiv:2505.06340](#)
- Hunt, L. K., Belfiore, F., Lelli, F., et al. 2023, *A&A*, 675, A64
- Inami, H., Algera, H. S. B., Schouws, S., et al. 2022, *MNRAS*, 515, 3126
- Inoue, A. K. 2011, *Earth, Planets and Space*, 63, 1027
- Ismail, D., Beelen, A., Buat, V., et al. 2023, *A&A*, 678, A27
- Jameson, K. E., Bolatto, A. D., Wolfire, M., et al. 2018, *ApJ*, 853, 111
- Jones, G. C., Bunker, A. J., Telikova, K., et al. 2024, *arXiv e-prints*, [arXiv:2405.12955](#)
- Kennicutt, R. C. & Evans, N. J. 2012, *ARA&A*, 50, 531
- Kennicutt, Jr., R. C. 1998, *ARA&A*, 36, 189
- Krumholz, M. R. 2012, *ApJ*, 759, 9
- Lang, P., Förster Schreiber, N. M., Genzel, R., et al. 2017, *ApJ*, 840, 92
- Lee, L. L., Förster Schreiber, N. M., Price, S. H., et al. 2025, *ApJ*, 978, 14
- Leńniewska, A. & Michałowski, M. J. 2019, *A&A*, 624, L13
- Liao, C.-L., Chen, C.-C., Wang, W.-H., et al. 2024, *ApJ*, 961, 226
- Lower, S., Narayanan, D., Hu, C.-Y., & Privon, G. C. 2024, *ApJ*, 965, 123
- Madau, P. & Dickinson, M. 2014, *ARA&A*, 52, 415
- Madden, S. C., Cormier, D., Hony, S., et al. 2020, *A&A*, 643, A141
- Madden, S. C., Geis, N., Genzel, R., et al. 1993, *ApJ*, 407, 579
- Magnelli, B., Lutz, D., Santini, P., et al. 2012a, *A&A*, 539, A155
- Magnelli, B., Saintonge, A., Lutz, D., et al. 2012b, *A&A*, 548, A22
- Mauerhofer, V., Dayal, P., Haehnelt, M. G., et al. 2025, *A&A*, 696, A157
- McMullin, J. P., Waters, B., Schiebel, D., Young, W., & Golap, K. 2007, in *Astronomical Society of the Pacific Conference Series*, Vol. 376, *Astronomical Data Analysis Software and Systems XVI*, ed. R. A. Shaw, F. Hill, & D. J. Bell, 127
- Michałowski, M. J. 2015, *A&A*, 577, A80
- Mitsuhashi, I., Tadaki, K.-i., Ikeda, R., et al. 2024, *A&A*, 690, A197
- Mitsuhashi, I., Zavala, J. A., Bakx, T. J. L. C., et al. 2025, *arXiv e-prints*, [arXiv:2501.19384](#)
- Moulet, A., Kataria, T., Lis, D., et al. 2023, *arXiv e-prints*, [arXiv:2310.20572](#)
- Pavesi, R., Riechers, D. A., Faisst, A. L., Stacey, G. J., & Capak, P. L. 2019, *ApJ*, 882, 168
- Popping, G., Shivaie, I., Sanders, R. L., et al. 2023, *A&A*, 670, A138
- Popping, G., Somerville, R. S., & Galametz, M. 2017, *MNRAS*, 471, 3152
- Price, S. H., Shimizu, T. T., Genzel, R., et al. 2021, *ApJ*, 922, 143
- Rémy-Ruyer, A., Madden, S. C., Galliano, F., et al. 2014, *A&A*, 563, A31
- Rizzo, F., Vegetti, S., Fraternali, F., Stacey, H. R., & Powell, D. 2021, *MNRAS*, 507, 3952
- Rowland, L. E., Heintz, K. E., Algera, H., et al. 2025a, *arXiv e-prints*, [arXiv:2510.11351](#)
- Rowland, L. E., Hodge, J., Bouwens, R., et al. 2024, *MNRAS*, 535, 2068
- Rowland, L. E., Stefanon, M., Bouwens, R., et al. 2025b, *arXiv e-prints*, [arXiv:2501.10559](#)
- Sawant, P., Nanni, A., Romano, M., et al. 2025, *A&A*, 694, A82
- Schneider, R. & Maiolino, R. 2024, *A&A Rev.*, 32, 2
- Scoville, N., Aussel, H., Brusa, M., et al. 2007, *ApJS*, 172, 1
- Scoville, N., Lee, N., Vanden Bout, P., et al. 2017, *ApJ*, 837, 150
- Shapley, A. E., Cullen, F., Dunlop, J. S., et al. 2020, *ApJ*, 903, L16
- Sommovigo, L. & Algera, H. 2025, *arXiv e-prints*, [arXiv:2505.20105](#)
- Sommovigo, L., Ferrara, A., Pallottini, A., et al. 2022, *MNRAS*, 513, 3122
- Tacconi, L. J., Genzel, R., Saintonge, A., et al. 2018, *ApJ*, 853, 179
- Tacconi, L. J., Genzel, R., Smail, I., et al. 2008, *ApJ*, 680, 246
- Tacconi, L. J., Genzel, R., & Sternberg, A. 2020, *ARA&A*, 58, 157
- Tamura, Y., Mawatari, K., Hashimoto, T., et al. 2019, *ApJ*, 874, 27
- Telikova, K., González-López, J., Aravena, M., et al. 2024, *arXiv e-prints*, [arXiv:2411.09033](#)
- Teng, Y.-H., Chiang, I.-D., Sandstrom, K. M., et al. 2024, *ApJ*, 961, 42
- Tripodì, R., Feruglio, C., Fiore, F., et al. 2024, *arXiv e-prints*, [arXiv:2401.04211](#)
- Valentino, F., Fujimoto, S., Giménez-Arteaga, C., et al. 2024, *A&A*, 685, A138
- Vallini, L., Pallottini, A., Ferrara, A., et al. 2018, *MNRAS*, 473, 271
- Vallini, L., Pallottini, A., Kohandel, M., et al. 2025, *A&A*, 700, A117
- Vijayan, A. P., Clay, S. J., Thomas, P. A., et al. 2019, *MNRAS*, 489, 4072
- Villanueva, V., Herrera-Camus, R., González-López, J., et al. 2024, *A&A*, 691, A133
- Vizgan, D., Greve, T. R., Olsen, K. P., et al. 2022a, *ApJ*, 929, 92
- Vizgan, D., Heintz, K. E., Greve, T. R., et al. 2022b, *ApJ*, 939, L1
- Whitaker, K. E., Pope, A., Cybulski, R., et al. 2017, *ApJ*, 850, 208
- Witstok, J., Jones, G. C., Maiolino, R., Smit, R., & Schneider, R. 2023, *MNRAS*, 523, 3119
- Wolfire, M. G., Hollenbach, D., & McKee, C. F. 2010, *ApJ*, 716, 1191
- Wolfire, M. G., Vallini, L., & Chevalue, M. 2022, *ARA&A*, 60, 247
- Wuyts, S., Förster Schreiber, N. M., Wisnioski, E., et al. 2016, *ApJ*, 831, 149
- Zanella, A., Daddi, E., Magdis, G., et al. 2018, *MNRAS*, 481, 1976
- Zavala, J. A., Casey, C. M., Spilker, J., et al. 2022, *ApJ*, 933, 242
- Zhao, Y., Liu, J., Zhang, Z.-Y., & Bisbas, T. G. 2024, *ApJ*, 977, 46

- ¹ Institute of Astronomy and Astrophysics, Academia Sinica, 11F of Astronomy-Mathematics Building, No.1, Sec. 4, Roosevelt Rd, Taipei 106319, Taiwan, R.O.C.
e-mail: hsbalgera@asiaa.sinica.edu.tw
- ² Universidad de Concepción, Víctor Lamas 1290, Barrio Universitario, Concepción, Chile
- ³ Millennium Institute for Galaxies (MINGAL)
- ⁴ Instituto de Estudios Astrofísicos, Facultad de Ingeniería y Ciencias, Universidad Diego Portales, Av. Ejército 441, Santiago, Chile
- ⁵ Department of Space, Earth, & Environment, Chalmers University of Technology, Chalmersplatsen, SE-4 412 96 Gothenburg, Sweden
- ⁶ Department of Astronomy and Joint Space-Science Institute, University of Maryland, College Park, MD 20854
- ⁷ Leiden Observatory, Leiden University, NL-2300 RA Leiden, the Netherlands
- ⁸ International Centre for Radio Astronomy Research, University of Western Australia, 35 Stirling Hwy, Crawley 26WA 6009, Australia
- ⁹ Canadian Institute for Theoretical Astrophysics, 60 St George St, University of Toronto, Toronto, ON M5S 3H8, Canada
- ¹⁰ David A. Dunlap Department of Astronomy and Astrophysics, University of Toronto, 50 St George St, Toronto ON M5S 3H4, Canada
- ¹¹ Department of Physics, 60 St George St, University of Toronto, Toronto, ON M5S 3H8, Canada
- ¹² Sterrenkundig Observatorium, Ghent University, Krijgslaan 281 S9, B-9000 Ghent, Belgium
- ¹³ Institute of Astrophysics, Foundation for Research and Technology Hellas (FORTH), Heraklion, GR-70013, Greece
- ¹⁴ School of Sciences, European University Cyprus, Diogenes street, Engomi, 1516 Nicosia, Cyprus
- ¹⁵ Caltech/IPAC, MS 314-6, 1200 E. California Blvd. Pasadena, CA 91125, USA
- ¹⁶ Scuola Normale Superiore, Piazza dei Cavalieri 7, 56126, Pisa, Italy
- ¹⁷ Max-Planck-Institut für Extraterrestrische Physik (MPE), Giessenbachstr., 85748, Garching, Germany
- ¹⁸ Space Telescope Science Institute, 3700 San Martin Drive, Baltimore, MD 21218, USA
- ¹⁹ Department of Astronomical Science, SOKENDAI (The Graduate University for Advanced Studies), Mitaka, Tokyo 181-8588, Japan
- ²⁰ National Astronomical Observatory of Japan, 2-21-1 Osawa, Mitaka, Tokyo 181-8588, Japan
- ²¹ Hiroshima Astrophysical Science Center, Hiroshima University, 1-3-1 Kagamiyama, Higashi-Hiroshima, Hiroshima 739-8526, Japan
- ²² Kavli Institute for Cosmology, University of Cambridge, Madingley Road, Cambridge CB3 0HA, UK
- ²³ Cavendish Laboratory, University of Cambridge, 19 JJ Thomson Avenue, Cambridge CB3 0HE, UK
- ²⁴ National Radio Astronomy Observatory, 520 Edgemont Road, Charlottesville, VA 22903, USA
- ²⁵ Dept. Física Teórica y del Cosmos, Universidad de Granada, Granada, Spain
- ²⁶ Instituto Universitario Carlos I de Física Teórica y Computacional, Universidad de Granada, E-18071 Granada, Spain
- ²⁷ Max-Planck-Institut für Radioastronomie, Auf dem Hügel 69, 53121 Bonn, Germany
- ²⁸ INAF – Osservatorio Astronomico di Padova, Vicolo dell'Osservatorio 5, I-35122 Padova, Italy
- ²⁹ Center for Computational Astrophysics, Flatiron Institute, 162 5th Avenue, New York, NY 10010, USA
- ³⁰ INAF – Osservatorio di Astrofisica e Scienza dello Spazio di Bologna, Via Piero Gobetti, 93/3, I-40129 Bologna, Italy
- ³¹ Astronomy Centre, University of Sussex, Falmer, Brighton BN1 9QH, UK

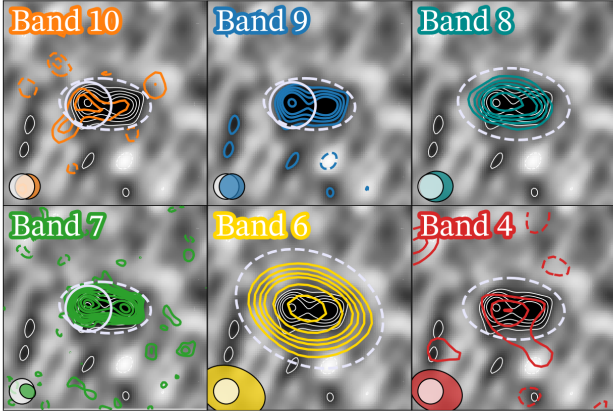


Fig. A.1. Six-band ALMA continuum maps of HZ10 ($4'' \times 4''$). Contours are drawn at 2, 3, 4, 5, 7 and 10σ , after which they continue in steps of 5σ . Negative contours are dashed. The synthesized beam of each observation is shown as a filled ellipse, and the Band 9 contours and synthesized beams are shown in white in each panel for reference. The apertures used for extracting the flux density of the full HZ10 system and – where possible – that of HZ10-C+E are shown as dashed and solid lavender regions, respectively.

Appendix A: Multi-band ALMA cutouts of HZ10

We show the ALMA continuum images of HZ10 in Bands 10 through 4 in Figure A.1. The Band 9 data were previously presented in Villanueva et al. (2024). The Band 8 and 6 observations were presented by Faisst et al. (2020), while the Band 7 observations are also shown in Telikova et al. (2024) and Herrera-Camus et al. (2025, here HZ10 is known as CRISTAL-22). The Band 10 and 4 observations are presented for the first time in this work.

Appendix B: Physical properties of HZ10 and HZ10-C+E

We present the multi-band ALMA flux measurements and other relevant physical parameters of HZ10 and HZ10-C+E in Table B.1.

Appendix C: Additional dust SED fits of HZ10

As discussed in Section 3, our fiducial fit to the ALMA photometry of HZ10 is that of an optically thin MBB (Figure 2). We compare this model to three additional fits in Figure C.1, adopting either a fixed optical depth of unity at $\lambda_{\text{thick}} = 100 \mu\text{m}$ (upper right panel), a varying optical depth (lower left), or optically thin, multi-temperature dust (lower right).

For the fit with fixed optical depth, we adopt $\lambda_{\text{thick}} = 100 \mu\text{m}$ following earlier work on HZ10 by Faisst et al. (2020) and Villanueva et al. (2024). Compared to our fiducial optically thin fit, we find a larger dust temperature of $T_{\text{dust}} = 51_{-7}^{+8}$ K (c.f., $T_{\text{dust}} = 37_{-5}^{+6}$ K), consistent with these earlier studies. The inferred dust mass of $\log(M_{\text{dust}}/M_{\odot}) = 7.8 \pm 0.2$ is furthermore consistent with our fiducial value of $\log(M_{\text{dust}}/M_{\odot}) = 8.0 \pm 0.1$ within the uncertainties. The recovered dust emissivity index of $\beta_{\text{IR}} = 2.2 \pm 0.3$ is similarly consistent with our fiducial fit.

For the fit with varying optical depth, we adopt a flat prior on the logarithm of the wavelength where the dust turns optically thick of $\log(\lambda_{\text{thick}}/\mu\text{m}) \in [-1, 3]$. This wide prior is chosen to allow for the possibility of both mostly optically thin dust ($\lambda_{\text{thick}} \ll 100 \mu\text{m}$), and an optical depth beyond what was assumed by Faisst et al. (2020) and Villanueva et al. (2024). We find that λ_{thick} cannot be well constrained by our fit, and

recover a bimodal distribution with either 1) mostly optically thin dust with a low temperature of $T_{\text{dust}} \sim 35$ K, or 2) dust that is optically thick out to $\lambda_{\text{thick}} \sim 150 \mu\text{m}$ with a warm temperature of $T_{\text{dust}} \gtrsim 50$ K. The median recovered value of $\log(\lambda_{\text{thick}}/\mu\text{m}) = 1.44_{-1.65}^{+0.80}$ corresponds to a wide range of possible values of $\lambda_{\text{thick}} \lesssim 170 \mu\text{m}$. This translates into large uncertainties on both the dust temperature ($T_{\text{dust}} = 43_{-9}^{+36}$ K) and the dust mass ($\log(M_{\text{dust}}/M_{\odot}) = 7.9_{-0.5}^{+0.2}$). However, both of these values are consistent with our fiducial optically thin values.

Finally, we apply a fit with a multi-temperature, optically thin dust distribution following Sommovigo & Algera (2025). Briefly, this assumes that the dust temperature distribution of HZ10 can be modeled as a skewed lognormal distribution represented by a mass-weighted dust temperature (T_{dust}), a standard deviation (σ_T) and skewness (ξ). All three parameters, as well as the dust mass and emissivity index, are varied in the fit, adopting the same priors as in Algera et al. (in preparation). From this multi-temperature model, we infer a mass-weighted dust temperature of $\langle T_d \rangle_{\text{MW}} = 29_{-7}^{+9}$ K, and a luminosity-weighted one of $\langle T_d \rangle_{\text{LW}} = 40_{-6}^{+9}$ K. We moreover infer a dust mass of $\log(M_{\text{dust}}/M_{\odot}) = 8.2_{-0.2}^{+0.3}$.

Comparing the four models, we find that the recovered dust temperatures, masses, emissivity indices and infrared luminosities are all consistent with each other within the uncertainties. This motivates our adoption of the optically thin dust model as fiducial, with a dust mass of $\log(M_{\text{dust}}/M_{\odot}) = 8.0 \pm 0.1$ – well within the range obtained from the three other models of $\log(M_{\text{dust}}/M_{\odot}) = 7.8 - 8.2$. As such, our analysis of the dust build-up in HZ10 in Section 4.2 does not strongly depend on which model for its dust emission is used.

Table B.1. ALMA continuum flux densities and relevant physical parameters of HZ10 and HZ10-C+E.

| | HZ10 | HZ10-C+E |
|---|-------------------------------|-------------------------------|
| $\lambda_{\text{obs}} [\mu\text{m}]$ | Flux [μJy] | Flux [μJy] |
| 2061 (Band 4) | 101 ± 42 | - |
| 1318 (Band 6) | 735 ± 98 | - |
| 1026 (Band 7) | 1529 ± 56 | 883 ± 37 |
| 738 (Band 8) | 2766 ± 414 | - |
| 447 (Band 9) | 3484 ± 487 | 1831 ± 326 |
| 348 (Band 10) | 3865 ± 1317 | 2797 ± 883 |
| $z_{[\text{C II}]}$ | 5.653 | 5.653 |
| $L_{[\text{C II}]} / (10^9 L_{\odot})^a$ | 5.88 ± 0.25 | 3.51 ± 0.20 |
| $L_{\text{CO}(2-1)} / (10^{10} \text{ K km s}^{-1} \text{ pc}^2)^b$ | 2.9 ± 0.6 | (1.7 ± 0.4) |
| $\log(M_{\star} / M_{\odot})^c$ | 10.35 ± 0.37 | (10.20 ± 0.22) |
| Z/Z_{\odot}^d | $0.53 - 0.71 (0.60 \pm 0.10)$ | $0.53 - 0.63 (0.60 \pm 0.10)$ |

Notes: Uncertainties on the flux densities are reported without the added calibration error (Section 2). When a range of measurements or no resolved measurements are available, we denote our adopted fiducial values in parentheses and in italics.

^(a) [C II]-based redshift and luminosity from [Herrera-Camus et al. \(2025\)](#). HZ10 and HZ10-C+E are denoted as CRISTAL-22 and CRISTAL-22a in their work, respectively.

^(b) CO(2-1) luminosity measured by [Pavesi et al. \(2019\)](#).

^(c) Stellar mass from [Mitsuhashi et al. \(2024\)](#).

^(d) The metallicity of the three components of HZ10 were measured individually by [Jones et al. \(2024\)](#), and range from $Z/Z_{\odot} = 0.53 \pm 0.09$ for HZ10-E to $Z/Z_{\odot} = 0.71 \pm 0.12$ for HZ10-C. We adopt a fiducial $Z/Z_{\odot} = 0.60 \pm 0.10$ based on these values.

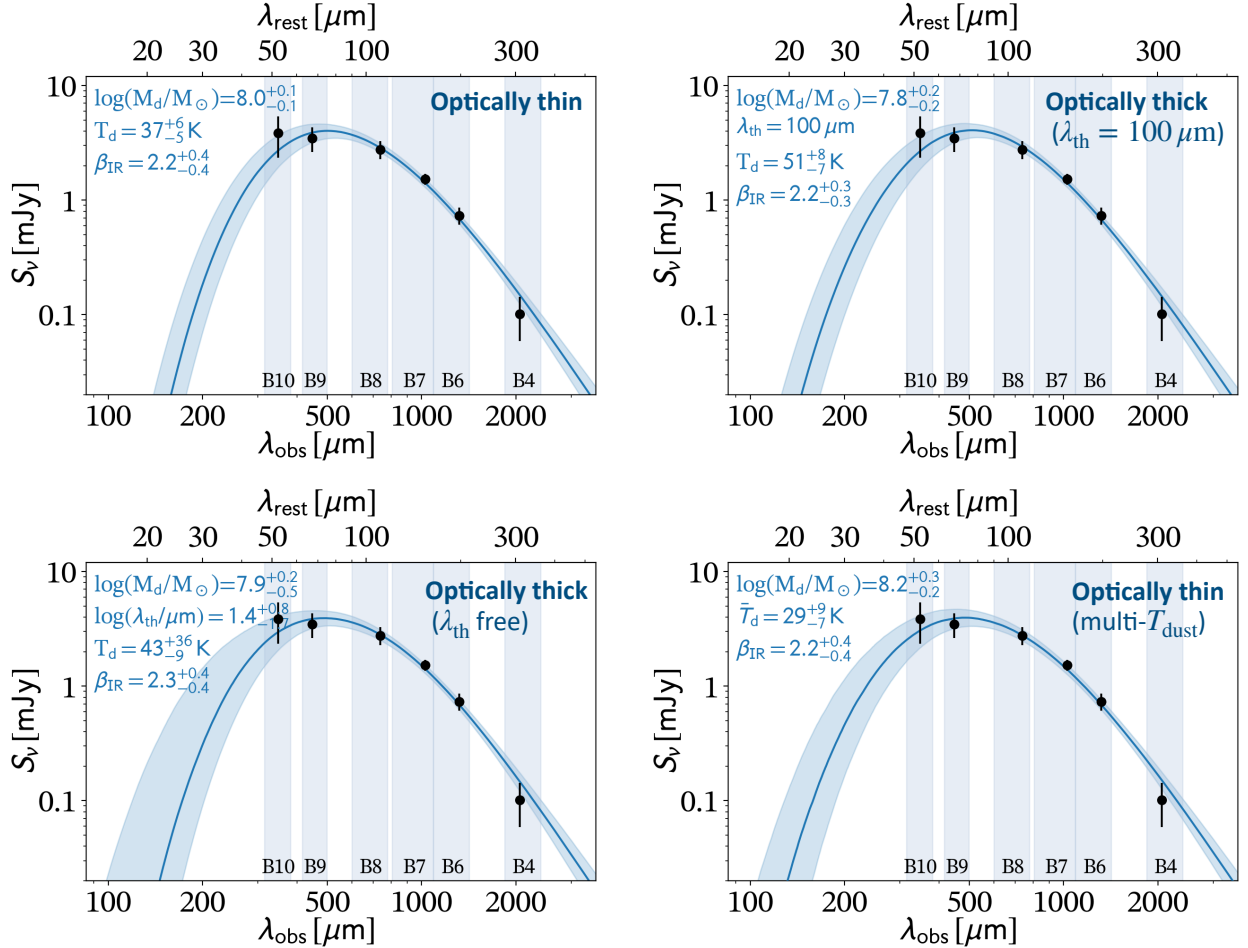


Fig. C.1. Four different fits to the ALMA continuum photometry of HZ10. *Upper left:* our fiducial optically thin fit, also shown in Figure 2. *Upper right:* a fit with fixed optical depth of unity at $\lambda_{\text{thick}} = 100 \mu\text{m}$, which has previously been assumed for HZ10 by [Faisst et al. \(2020\)](#) and [Villanueva et al. \(2024\)](#). *Lower left:* a fit with varying λ_{thick} . *Lower right:* an optically thin fit with multi-temperature dust, using the analytical prescription from [Sommovigo & Algera \(2025\)](#), see also Algera et al. in preparation). While the dust temperature depends on the assumption regarding optical depth, all models yield similar dust masses, emissivity indices, and infrared luminosities.